AGU ADVANCING EARTH AND SPACE SCIENCE

Geophysical Research Letters®

Key Points:

- The space weathering (SW) characteristics of lunar soils returned by Chang'e-5 landing at the mid-high latitude site are reported
- Microscopic textures of SW depend on mineral species but show no relationship with the latitude of sampling site
- The SW products by micrometeorite impacts and solar wind irradiation are distinguished

Supporting Information:

Supporting Information may be found in the online version of this article.

Correspondence to:

Y. Lin and J. Li,
LinYT@mail.iggcas.ac.cn;
lijinhua@mail.iggcas.ac.cn

Space Weathering of the Chang'e-5 Lunar Sample From a Mid-High Latitude Region on the Moon

HPSTAR
1614-2022

Lixin Gu[1], Yongjin Chen[2], Yuchen Xu[3], Xu Tang[1], Yangting Lin[1,4] (ORCID), **Takaaki Noguchi[5], and Jinhua Li[1,4]** (ORCID)

[1]Key Laboratory of Earth and Planetary Physics, Institute of Geology and Geophysics, Chinese Academy of Sciences, Beijing, China, [2]Center for High Pressure Science & Technology Advanced Research, Beijing, China, [3]State Key Laboratory of Space Weather, National Space Science Center, Chinese Academy of Sciences, Beijing, China, [4]College of Earth and Planetary Sciences, University of Chinese Academy of Sciences, Beijing, China, [5]Faculty of Arts and Science, Kyushu University, Fukuoka, Japan

Abstract Micrometeorite impacts and solar wind irradiation, the dominant space weathering (SW) processes, largely modified compositions and microtexture of soil materials on the Moon. Here, we report the SW characteristics of the Chang'e-5 lunar soils from mid-high latitude ($43.06°N$). All mineral phases exposed on the surface of a single basalt clast have a vapor deposit layer, whereas the textures of the solar wind irradiation-damaged zone are dependent on the host mineral species. Nanophase Fe ($npFe^0$) particles are spherical in the amorphized zone of pyroxenes, elongated in ilmenite, and irregular on the jagged surface of iron sulfide, but not found in Fe-poor merrillite. Vesicles were found in the damaged zone of ilmenite and merrillite, but with different shapes. The observations were compared to Apollo samples and demonstrate no significant altitude-dependent effects on the SW, which is important for decoding the reflectance spectra of the Moon.

Plain Language Summary The lunar surface has been suffering intense meteorite impacts and solar wind irradiation for billions of years, which heavily modifies its physical properties, chemical compositions and mineralogical features, and in turn, the optical reflectance spectra of the Moon. The meteorite impacts are random events, but the intensity of solar wind irradiation is latitude dependent. However, all Apollo and Luna missions landed in a narrow and low range of lunar latitude. The Chang'e-5 (CE-5) mission returned lunar soil samples from a middle latitude ($43.06°N$), providing unique samples for study of lunar space weathering (SW). In this paper, we report the SW features of various minerals from a single basaltic clast of the CE-5 sample. Our observations reveal phase-dependent effects on the SW. Furthermore, the CE-5 lunar soil shows no significant differences from those of Apollo samples, suggestive of little latitude-dependent effects on lunar SW.

1. Introduction

The optical properties, chemical compositions and mineralogical features of the surface materials on the Moon and other airless celestial bodies have been highly altered by space weathering, including impact by meteorites and micrometeorites and irradiation by solar wind and cosmic rays (Hapke, 2001; Keller & McKay, 1993, 1997). The impacting events cause melting, vapourization, recondensation and gardening of the regolith (Laczniak et al., 2021). On the other hand, solar wind ions (mostly H^+ and He^+) implant into the surface materials, resulting in the formation of defective, amorphous and/or vesicle-bearing zones that preserve the same compositions of the host minerals (Harries & Langenhorst, 2014; Keller & McKay, 1997; Noguchi et al., 2011). Both dominant processes of space weathering, that is, micrometeorite impact and solar wind implantation, can produce nanophase Fe ($npFe^0$) particles, which were considered to be the main cause for large modification of the reflectance spectra of airless surfaces (Cassidy & Hapke, 1975; Pieters & Noble, 2016). However, Only a few studies reported the space weathering behaviors of different phases under the same exposure environment (Burgess & Stroud, 2018; Matsumoto et al., 2015). In addition, solar wind irradiation on the Moon is latitude-dependent, which could be the key factor for the global lunar distribution of OH/H_2O (Li & Milliken, 2017). However, the Apollo and Luna samples were collected from a narrow range of latitude ($0 \pm 23°$). Study of new samples returned from a higher-latitude region on the Moon provides a unique opportunity to study the effects of latitude on space weathering.
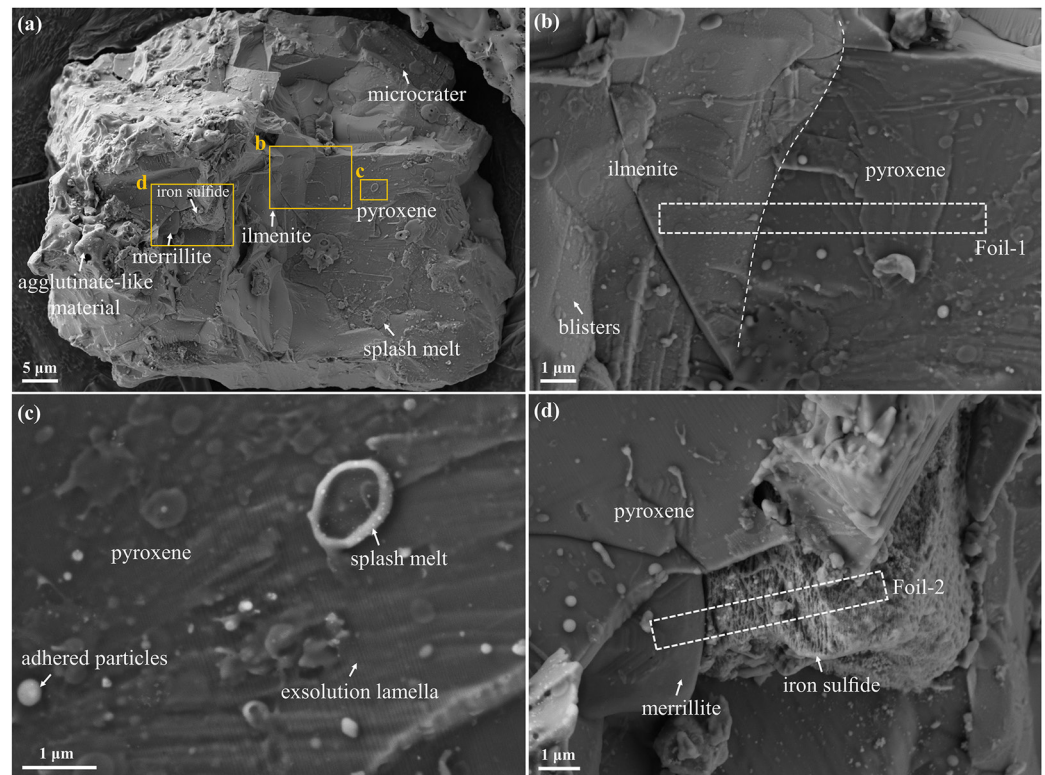
Figure 1. Surface morphology of the lunar soil grain. (a) The grain consists of pyroxene, ilmenite, merrillite and iron sulfide. Agglutinate-like material, splash melt and a microcrater are readily observed. The positions of detailed surface morphology are marked by the orange squares. (b) The surface morphology of pyroxene and ilmenite. Abundant blisters are observed on the surface of ilmenite. The dotted square area containing pyroxene and ilmenite was selected for focused ion beam cuttering (Foil-1). (c) Pyroxene shows exsolution lamella texture. (d) The surface morphology of merrillite and iron sulfide. The iron sulfide shows an irregular honeycomb-like rough surface with tiny particles. The dotted square shows the region where Foil-2 was extracted.

The Chang'e-5 (CE-5) mission, the first lunar sample return mission since 1976, has brought back new soil samples from the mid-high latitude region (43.06°N) in the northeastern Oceanus Procellarum (Yang & Lin, 2021). The CE-5 soil samples are predominated by the youngest mare basalt clasts dated 2.0 Ga (Li et al., 2021; Tian et al., 2021). In this work, we conducted a morphological, mineralogical, and crystallographic study on a single basalt clast of typical CE-5 lunar soil samples, with most of the constituent minerals exposed on the grain surface. These minerals, including high-Ca pyroxene with exsolution of low-Ca pyroxene, ilmenite, iron sulfide and merrillite, have experienced space weathering under identical condition. Our discoveries shed light on the relationship between space weathering features and various minerals, and clearly distinguish the impact-induced products from the solar wind irradiation-derived ones.

2. Samples and Methods

The CE-5 lunar soil grains used in this study were from an aliquot sample (CE5C0400YJFM00407; CE5C0400Y-JFM00405) allocated by China National Space Administration. Particle analysis were carried out following the technical roadmap established by (Li et al., 2022). Tens of grains were transferred on a conductive carbon tape on a sample mount. They were coated with carbon (~10 nm thick), and observed with a Thermo Fisher Apreo scanning electron microscope (SEM) and a Zeiss Auriga Compact focused ion beam scanning electron microscope (FIB-SEM) at the Institute of Geology and Geophysics, Chinese Academy of Sciences (IGGCAS). Based on the SEM observation, a multi-phase clast (labeled as S01-004; Figure 1a) was selected for transmission electron microscopy (TEM) analysis.

Two ultra-thin foils (~100 nm in thickness) were prepared using the Zeiss Auriga Compact FIB-SEM at IGGCAS. Ion beam conditions for milling and final polishing were 5–30 kV high voltage with various beam currents (20 pA–4 nA). Foil-1 crossed the boundary between ilmenite and pyroxene (Figure 1b), while Foil-2 contains adjacent merrillite and iron sulfide (Figure 1d). Before the FIB-cutting, Pt was deposited to protect the sample surface from any focused ion beam (FIB) Ga^+ damage during the cutting and milling processes.

TEM analysis was conducted with a JEOL JEM-2100 at IGGCAS and another JEOL JEM-F200 field emission TEM at the Center for High Pressure Science & Technology Advanced Research, Beijing. Crystallographic structures were analyzed by selected area electron diffraction (SAED), high resolution TEM imaging (HRTEM) and high angle annular dark field scanning transmission electron microscopy (HAADF-STEM). Energy dispersive x-ray spectroscopy (EDS) data were collected to analyze chemical compositions of the samples. More details of TEM experiments are provided in the in Supporting Information S1.

3. Results and Discussion

### 3.1. Space Weathering-Derived Surface Morphology

The selected CE-5 lunar soil grain contains high-Ca and low-Ca pyroxenes, ilmenite, merrillite and iron sulfide on the exposed surface (Figure S1; Table S1 in Supporting Information S1). The high-Ca ($Fs_{35}Wo_{39}$) and low-Ca ($Fs_{64}Wo_1$) pyroxenes occur as lamellae with different contrast in the SEM images, and the widths of both high-Ca and low-Ca pyroxene lamellae range from 10 to 30 nm (Figures 1c and 2b and Figure S2 in Supporting Information S1). The surface of ilmenite shows abundant blisters (tens of nanometer in size) (Figure 1b). The iron sulfide has a irregular honeycomb-like rough surface, with tiny $npFe^0$ particles on the surface (Figures 1d and 3d and Figure S5 in Supporting Information S1). The surface of merrillite is smooth, without notable features. Agglutinate-like material, splash melts, microcraters and numerous adhered tiny particles are readily observed on the surface of the grain without correlation with the underlying minerals.

The space weathering-derived surface morphology can be further observed with TEM of the ultra-thin foils. There is a thin vapor deposit layer on the topmost surface of the clast, covering all the constituent minerals (Figure S2–S5 in Supporting Information S1). The thickness of the vapor deposit layer is ~10 nm on the surfaces of pyroxene (Figure 2b; Figure S2 in Supporting Information S1), ilmenite (Figure 2f; Figure S3 in Supporting Information S1) and merrillite (Figure S4 in Supporting Information S1), whereas it has a wide range from undetectable to tens of nanometers on the rough surface of iron sulfide (Figure S5 in Supporting Information S1). A vapor deposit layer has been reported for the Apollo soil samples (e.g., Keller & McKay, 1993, 1997) and Itokawa asteroid dust grains (e.g., Noguchi et al., 2014; Thompson et al., 2014). It could be condensed following either solar wind sputtering and/or micrometeorite impact vapourization (Hapke, 2001; Keller & McKay, 1997). The vapor deposit layer is more Si-rich than the underlying host materials (Figure S2–S5 in Supporting Information S1), an important feature that distinguishes it from the solar wind damaged zone discussed below in detail. In addition, $npFe^0$ particles were identified only on ilmenite, where the vapor deposit layer shows a small island morphology (Figure 2e). The $npFe^0$ particles in the vapor deposit layer of ilmenite are spherical in shape and small in size (with an average diameter of 4.7 ± 0.8 nm, n = 8) (Figure 4c).

3.2. Solar Wind Irradiation-Damaged Zones of Various Minerals

Below the vapor deposit layer, there is the solar wind irradiation-damaged zone, in which the observed space weathering features include amorphorization, $npFe^0$ particles and vesicles. Full amorphorization induced by solar wind irradiation was found only in pyroxene. The amorphized zone (~50 nm in thickness) retains the same parallel lamella texture with the identical compositions of the underlying host pyroxenes in STEM-HAADF images (Figure 2b; Figure S2 in Supporting Information S1), providing robust evidence that solar wind irradiation, instead of micrometeorite impacts, created it. This clast has an exposure age of $\sim 3.2 \times 10^5$ years (Figure S8 in Supporting Information S1), estimated from the solar flare track density in pyroxene based on a 2π track production rate of $4.4 \pm 0.4 \times 10^4$ tracks cm^{-2} yr^{-1} at 1 AU (Keller et al., 2021). Ilmenite and merrillite have significantly thicker solar wind-damaged zones, ~80 nm (Figure 2e) and ~160 nm (Figure 3b), respectively, but the HRTEM images of them show lattice fringes extending to the topmost surface. The same texture has been observed in olivine (Keller et al., 2021). The retaining of crystal structures is related to the radiation resistance of different minerals (Burgess & Stroud, 2018; Keller et al., 2021; Wirth, 2007), or the ion damage could be rapidly
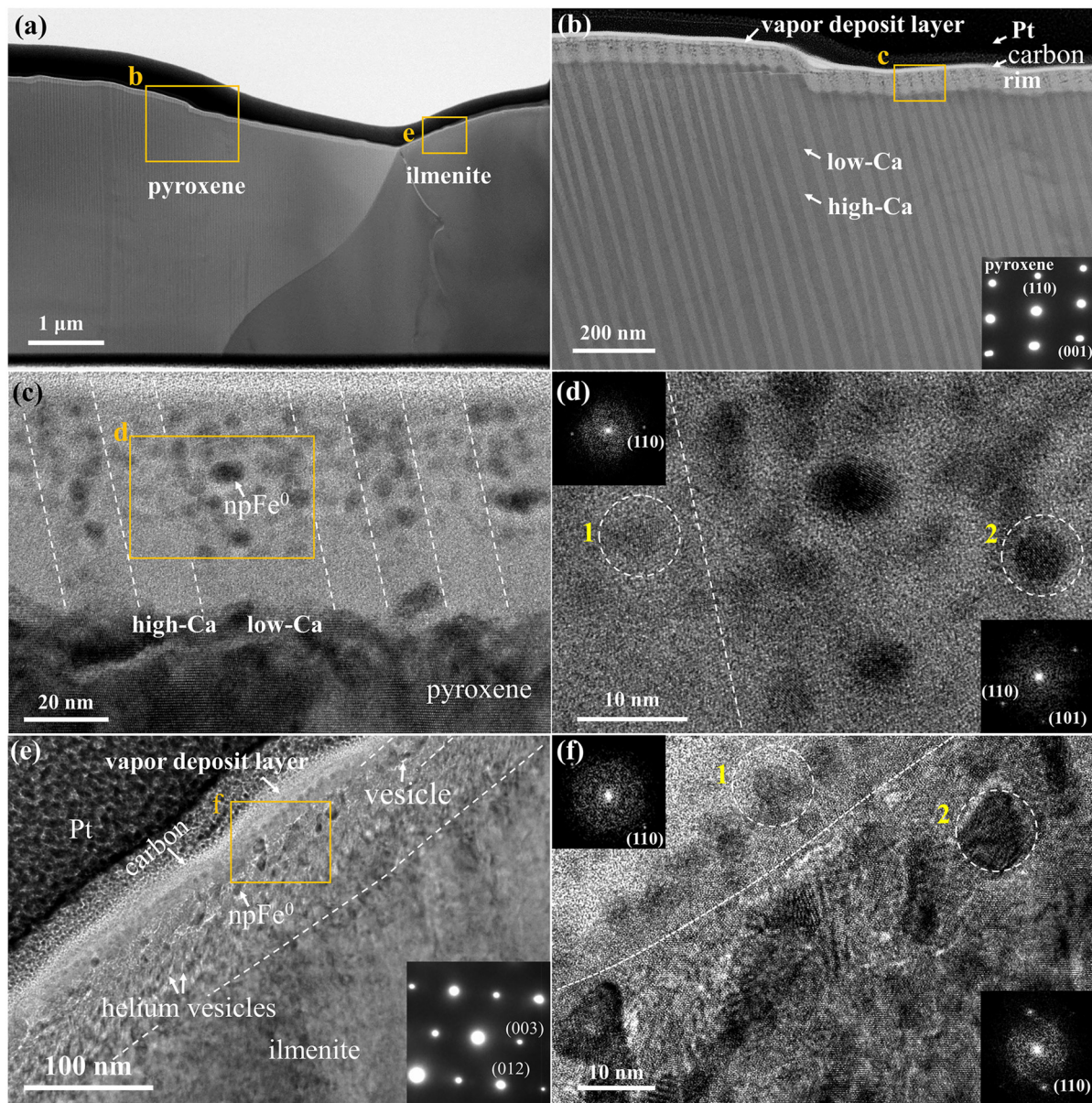
Figure 2. Microstructure of pyroxene and ilmenite in Foil-1. (a) High angle annular dark field image of Foil-1. (b) Transmission electron microscopy (TEM) image of pyroxene displays a thin vapor deposit layer and space weathered rim (~50 nm) beneath the coatings. Pyroxene shows clear parallel exsolution lamella with the width ranging from 10 to 30 nm. (c) High resolution TEM (HRTEM) image of the region marked in (b) reveals that $npFe^0$ are relatively more abundant and larger in the solar wind damaged zone of low-Ca pyroxene lamellae than those in the high-Ca pyroxene lamellae. (d) HRTEM image and the corresponding FFT image of $npFe^0$ in high-Ca and low-Ca pyroxene lamella, respectively. (e) TEM image of ilmenite surface. A vapor deposit layer is present beneath the coatings and shows an island-like morphology. Below the vapor deposit, the solar wind damaged zone (~80 nm) contains irregular vesicles coexisting with $npFe^0$ particles in the upper part, and parallel helium vesicles in the $npFe^0$-free lower part. The elongation direction of helium vesicles is parallel to the (001) plane of ilmenite. (f) HRTEM image and its corresponding FFT image of ilmenite, showing $npFe^0$ particles in the vapor deposit layer (encircled as 1) and solar wind damaged zone (encircled as 2).

annealed by diurnal heating on the lunar surface. Unlike silicates, phosphate and ilmenite, the iron sulfide was found to have a unique jagged surface, with no obvious solar wind-damaged zone.

Ni-free $npFe^0$ particles were found in the solar wind-damaged zone of all the minerals observed in this study, except for Fe-poor merrillite. Furthermore, the occurrences of $npFe^0$ depend on the host mineral species. The $npFe^0$ particles are spherical in the amorphized zone of pyroxene (Figures 2c and 2d), whereas they are irregular in the upper part of solar wind damaged zone of ilmenite (Figures 2e and 2f), and as iron whiskers on the jagged surface of iron sulfide (Figures 3a and 3d and Figure S5 in Supporting Information S1). In addition, the sizes
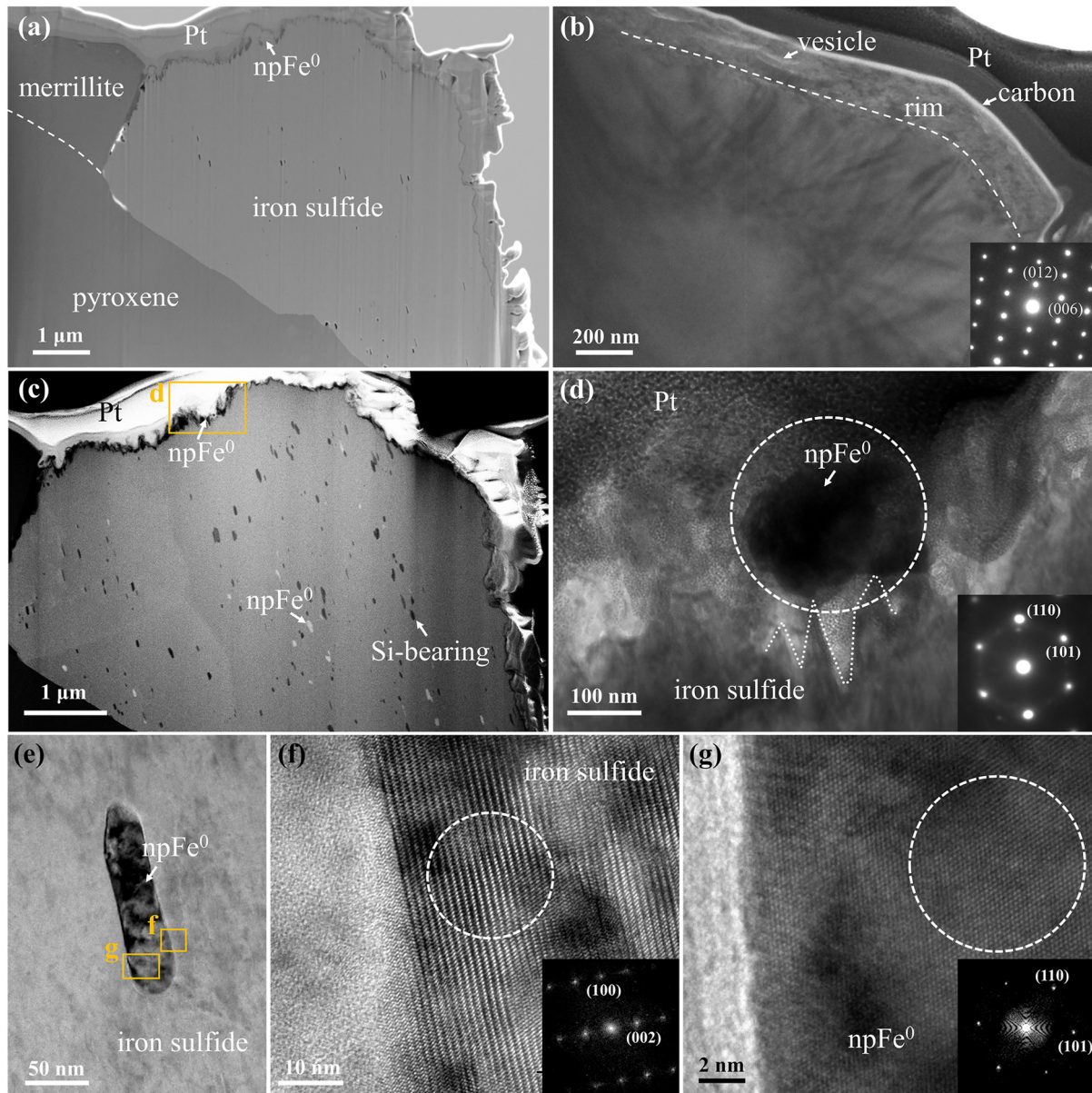
Figure 3. Microstructure of merrillite and iron sulfide in Foil-2. (a) The secondary electron image of Foil-2. The iron sulfide shows a jagged surface with several tiny particles. (b) The solar wind damaged zone of merrillite is ∼160 nm in thickness and shows vesicular structure. (c) High angle annular dark field image shows the distribution of $npFe^0$ particles (bright contrast) in the interior of iron sulfide. The dark regions are vesicles and Si-bearing inclusions. (d) Transmission electron microscopy (TEM) image of $npFe^0$ on the surface of iron sulfide and its corresponding selected area electron diffraction pattern. (e) TEM image of $npFe^0$ inside the iron sulfide. (f) high resolution TEM (HRTEM) image of interface between iron sulfide and $npFe^0$ marked in (e) shows the elongation direction of $npFe^0$ is aligned with the (001) plane of iron sulfide (indexed as troilite). (g) HRTEM of $npFe^0$ marked in (e) and its corresponding FFT image.

of $npFe^0$ particles are variable. The HRTEM observations reveal that $npFe^0$ are larger in the low-Ca, high-Fe pyroxene lamellae (with an average diameter of 4.6 ± 0.7 nm, n = 11) than those in the high-Ca, low-Fe pyroxene lamellae (with an average diameter of 3.5 ± 0.8 nm, n = 10) (Figures 4a and 4b). In ilmenite, the $npFe^0$ particles are significantly larger (with an average length of ∼11.7 nm and a width of ∼6.2 nm) than those in pyroxenes (Figure 4d). The $npFe^0$ particles on the jagged surface of iron sulfide are the largest, ranging from tens of nanometers to ∼300 nm in length (Figure 4e). The maximum depth of the presence of $npFe^0$ particles is variable for different host minerals. The $npFe^0$ particles are present in nearly the whole amorphized zone (∼40 nm in thickness) of low-Ca, high-Fe pyroxene lamellae, but only in the upper part (∼35 nm) of those in the high-Ca, low-Fe pyroxene lamellae (Figure 4g). In the solar wind damaged zone of ilmenite, the maximum depth of $npFe^0$ is ∼40 nm from
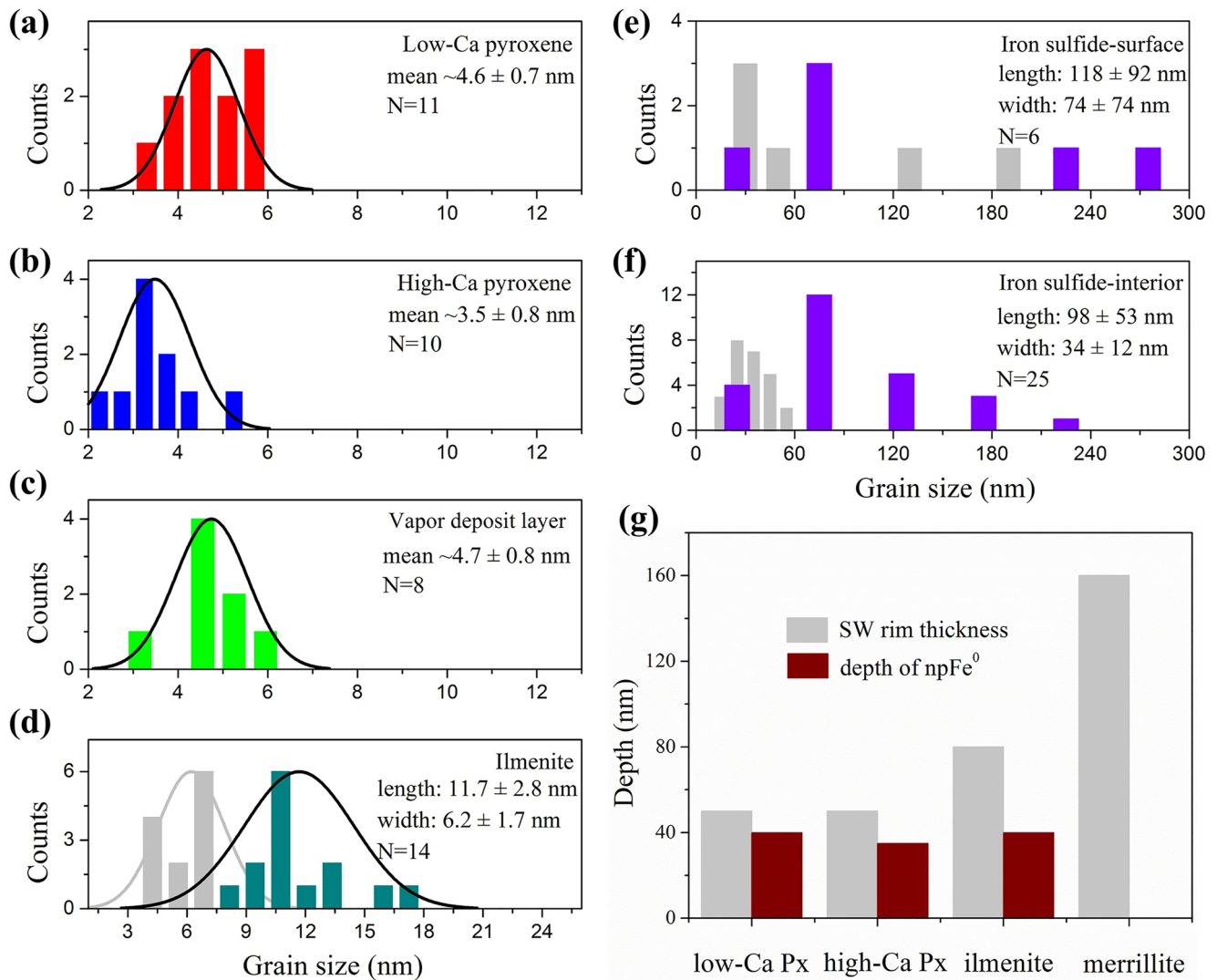
Figure 4. The size and depth histograms of npFe^0 particles in the solar wind damaged zone of various minerals. (a) Low-Ca pyroxene lamellae; (b) high-Ca pyroxene lamellae; (c) vapor deposit layer on the surface of ilmenite; (d) solar wind damaged zone of ilmenite; (e) iron sulfide surface; (f) iron sulfide interior. Gray-colored data in (d, e, and f) are for width compared to colored data for length. The figures used to measure the size of npFe^0 particles include Figures 2 and 3, Figures S5 and S9 in Supporting Information S1. (g) The thickness of space weathering damaged zone (gray), and the depth of the presence of npFe^0 particles (red).

the top surface (Figure 4g). The observed maximum depth of npFe^0 (~40–50 nm) is consistent with the stopping depth of 1 keV H$^+$ ions (Christoffersen et al., 1996), indicative of possible correlation of npFe^0 particles with the implanted solar wind H$^+$. The STEM-EDS mapping of ilmenite reveals the presence of Ti-enriched regions adjacent to the npFe^0 particles (Figure S3 in Supporting Information S1), indicating possible separation of Fe and Ti during the space weathering process as reported in previous studies (Burgess & Stroud, 2018; Christoffersen et al., 1996; Zhang & Keller, 2010). The npFe^0 particles on the jagged surface of iron sulfide protrude from the surface mainly due to solar wind sputtering and consequent growth of the crystals, which is similar to iron whiskers observed in the Apollo lunar soils and the asteroid Itokawa dust grains (Matsumoto et al., 2020, 2021).

For the first time in a natural sample, npFe^0 was found in iron sulfide as elongated nanoparticles distributed throughout the interior (Figures 3c and 3e–3g). There are vesicles and tiny Si-bearing inclusions coexisting with npFe^0 particles in the interior of iron sulfide (Figure 3c; Figure S5–S7; Table S1 in Supporting Information S1). However, we cannot exclude the possibility that the vesicles were an artifact due to loss of pre-existing Si-bearing inclusions during the FIB milling process. The elongated npFe^0 particles show a crystallographic orientation aligned with the (001) plane of the host iron sulfide (Figure 3f). The sizes of the npFe^0 particles vary from tens
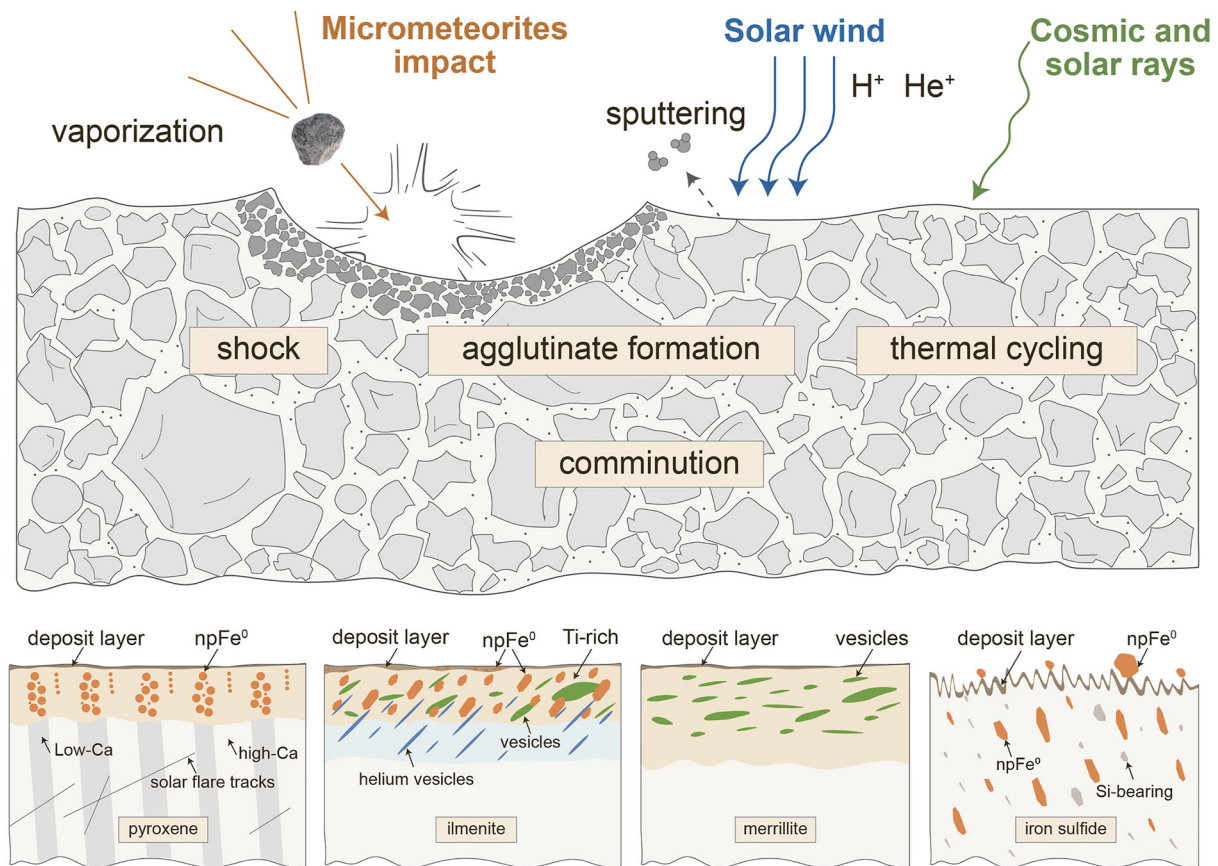
Figure 5. (a) The constituent processes involved in space weathering (SW) of airless bodies modified from (Pieters & Noble, 2016; Thompson et al., 2021) and schematic representation of the SW features of pyroxene, ilmenite, merrillite and iron sulfide in this study.

of nanometers to ~200 nm in length (Figure 4f). They could not be produced by solar wind irradiation, because they reside too deep within the host iron sulfide for solar wind ions to implant. It is possible that the co-existing $npFe^0$ and Si-bearing inclusions resulted from immiscible liquids in an igneous system or produced by meteorite impact-induced melting.

Vesicles were observed in the solar wind damaged zones of ilmenite (Figures 2e and 2f) and merrillite (Figure 3b). The vesicles in merrillite are irregular, whereas those in ilmenite occur in two forms, that is, irregular ones coexisting with $npFe^0$ in the upper part of solar wind damaged zone, and the parallel helium vesicles in the lower $npFe^0$-free part (Figure 2e). The irregular vesicles (up to tens nanometers) are related with the presence of blisters visible on the surface of ilmenite, attributed to accumulation of the implanted solar wind H and/or He ions (Assonov et al., 1998; Burgess & Stroud, 2021; Christoffersen et al., 1996; Matsumoto et al., 2015; Muto & Enomoto, 2005; Noguchi et al., 2014). The vesicles in the lower part are long, narrow, and oriented parallel to (001) plane of the host ilmenite (Figure 2e). The maximum depth of the parallel vesicles is up to 80 nm, which could be induced by the implantation of solar wind He^+ ions as reported in previous studies (Burgess & Stroud, 2018; Christoffersen et al., 1996).

3.3. A Space Weathering Model for the CE-5 Lunar Soils

The multi-phase clast from the CE-5 lunar soil demonstrates the complicated space weathering on the Moon's surface. Most of the space weathering features can be summarized in Figure 5. The surface of the space weathered clast is characteristic of the presence of agglutinate-like material, splash melts, microcraters and numerous adhered tiny particles, mostly related to micrometeorite impacting process. Iron sulfide shows a unique irregular honeycomb-like rough surface, providing convincing evidence for sputtering loss by solar wind ions. Both micrometeorite impact and solar wind sputtering could contribute to the vapor deposit layer on the topmost surface

of lunar soil grains, observed by SEM and TEM. Spherical $npFe^0$ particles were found within the vapor deposit layer only on ilmenite, where the vapor deposit layer shows an island-like morphology and appears like splash melt produced by micrometeorite impact.

Beneath the vapor deposit layer, all the space weathering features can be attributed to solar wind irradiation, including amorphization and the presence of $npFe^0$ particles and vesicles. However, these space weathering features are phase-dependent. $NpFe^0$ particles are more abundant and coarser in the amorphized zone of low-Ca, high-Fe pyroxene lamellae than those in the high-Ca, low-Fe pyroxene lamellae. They are elongated (up to 20 nm in length) in the solar wind damaged zone of ilmenite, and irregular (up to 300 nm in length) on the jagged surface of iron sulfide, but not found in the Fe-poor merrillite. The sizes and abundances of $npFe^0$ appear to be related with the Fe concentrations of the host minerals. The shape of $npFe^0$ particles is sometimes controlled by the crystallographic structure of the host ilmenite mineral, showing crystallographic orientation. Ilmenite and iron sulfide are more resistant to radiation-induced amorphization than pyroxene, resulting in the preferred orientation growth of $npFe^0$. Vesicles found here are mainly formed by solar wind implantation, but their shapes vary in different host minerals.

The observed space weathering features of the CE-5 samples are similar with those reported for the Apollo samples (Burgess & Stroud, 2018; Gu et al., 2018; Matsumoto et al., 2021), suggesting that latitudes of the sampling sites have little effect on space weathering on the Moon. This discovery is important for decoding the global remote sensing of the Moon. The thickness of the amorphized zone is usually related to the exposure ages of the sample until it achieves the steady-state value in a few Myr (Keller et al., 2021), and the observed amorphous zone thickness (average of 50–60 nm) appear typical for lunar soils (Keller & McKay, 1993, 1997). The sizes of $npFe^0$ particles in the amorphized zone of pyroxene and in the vapor deposit layer on ilmenite are similar to those in amorphous rims of Apollo lunar soils, ranging ~1–10 nm with an average diameter of ~3 nm (Gu et al., 2018; Keller & Clemett, 2001; Keller & McKay, 1997; Pieters et al., 2000). The larger irregular $npFe^0$ particles observed in ilmenite were reported in Apollo 17 samples, and were linked with possible heating events (Burgess & Stroud, 2018). The $npFe^0$ particles on the jagged surface of iron sulfide have been observed in Apollo 11 and Apollo 17 samples (Matsumoto et al., 2021), but the occurrence of $npFe^0$ particles in the interior of iron sulfide is reported here for the first time in a natural sample. Our results clearly distinguish impact-induced products from solar wind irradiation-derived features and shed light on the space weathering processes on the Moon. However, the similarity microscopic effects of space weathering do not imply identical OH/H_2O preserved at those latitudes. In addition, further studies combining the microstructural features and associated optical effects are of great important for exploring the Moon. When expanding the model of space weathering to other airless bodies, the target compositions and complexity of space environment should be considered due to the diversity of space weathering effects (Thompson et al., 2021; Zhang et al., 2022).

Conflict of Interest

The authors declare no conflicts of interest relevant to this study.

Data Availability Statement

The data used in this manuscript are available online (https://doi.org/10.5281/zenodo.6349937).

References

Assonov, S., Biryukov, A. Y., Kashkarov, L., Nevzorov, V., Semenova, A., & Shukolyukov, Y. A. (1998). Vesiculation in silicate grains of Luna-16 soil. *Lunar and Planetary Science Conference*. https://doi.org/10.1080/01619563409535205

Burgess, K. D., & Stroud, R. M. (2018). Phase-dependent space weathering effects and spectroscopic identification of retained helium in a lunar soil grain. *Geochimica et Cosmochimica Acta*, *224*, 64–79. https://doi.org/10.1016/j.gca.2017.12.023

Burgess, K. D., & Stroud, R. M. (2021). Comparison of space weathering features in three particles from Itokawa. *Meteoritics & Planetary Sciences*, *56*(6), 1109–1124. https://doi.org/10.1111/maps.13692

Cassidy, W., & Hapke, B. (1975). Effects of darkening processes on surfaces of airless bodies. *Icarus*, *25*(3), 371–383. https://doi.org/10.1016/0019-1035(75)90002-0

Christoffersen, R., Keller, L. P., & Mckay, D. S. (1996). Microstructure, chemistry, and origin of grain rims on ilmenite from the lunar soil finest fraction. *Meteoritics & Planetary Sciences*, *31*(6), 835–848. https://doi.org/10.1111/j.1945-5100.1996.tb02117.x

Gu, L., Zhang, B., Hu, S., Noguchi, T., Hidaka, H., & Lin, Y. (2018). The discovery of silicon oxide nanoparticles in space-weathered of Apollo 15 lunar soil grains. *Icarus*, *303*, 47–52. https://doi.org/10.1016/j.icarus.2017.12.028

Hapke, B. (2001). Space weathering from Mercury to the asteroid belt. *Journal of Geophysical Research*, *106*(E5), 10039–10073. https://doi.org/10.1029/2000JE001338

Harries, D., & Langenhorst, F. (2014). The mineralogy and space weathering of a regolith grain from 25143 Itokawa and the possibility of annealed solar wind damage. *Earth Planets and Space*, *66*, 163. https://doi.org/10.1186/s40623-014-0163-1

Keller, L., & Clemett, S. J. (2001). *Formation of nanophase iron in the lunar regolith, Lunar and Planetary Science Conference, 2097*.

Keller, L. P., Berger, E. L., Zhang, S., & Christoffersen, R. (2021). Solar energetic particle tracks in lunar samples: A transmission electron microscope calibration and implications for lunar space weathering. *Meteoritics & Planetary Sciences*, *56*(9), 1685–1707. https://doi.org/10.1111/maps.13732

Keller, L. P., & McKay, D. S. (1993). Discovery of vapor deposits in the lunar regolith. *Science*, *261*(3), 1305–1307. https://doi.org/10.1126/science.264.5166.1779

Keller, L. P., & McKay, D. S. (1997). The nature and origin of rims on lunar soil grains. *Geochimica et Cosmochimica Acta*, *61*(11), 2331–2341. https://doi.org/10.1016/S0016-7037(97)00085-9

Laczniak, D., Thompson, M., Christoffersen, R., Dukes, C., Clemett, S., Morris, R., & Keller, L. (2021). Characterizing the spectral, microstructural, and chemical effects of solar wind irradiation on the Murchison carbonaceous chondrite through coordinated analyses. *Icarus*, 114479. https://doi.org/10.1016/j.icarus.2021.114479

Li, J., Li, Q., Zhao, L., Zhang, J., Tang, X., Gu, L., et al. (2022). Rapid screening of Zr-containing particles from Chang'E-5 lunar soil samples for isotope geochronology: Technical roadmap for future study. *Geoscience Frontiers*, *13*(3), 101367. https://doi.org/10.1016/j.gsf.2022.101367

Li, Q.-L., Zhou, Q., Liu, Y., Xiao, Z., Lin, Y., Li, J.-H., et al. (2021). Two billion-year-old volcanism on the Moon from Chang'e-5 basalts. *Nature*, *600*(7887), 54–58. https://doi.org/10.1038/s41586-021-04100-2

Li, S., & Milliken, R. E. (2017). Water on the surface of the Moon as seen by the Moon mineralogy mapper: Distribution, abundance, and origins. *Science Advances*, *3*(9), e1701471. https://doi.org/10.1126/sciadv.1701471

Matsumoto, T., Harries, D., Langenhorst, F., Miyake, A., & Noguchi, T. (2020). Iron whiskers on asteroid Itokawa indicate sulfide destruction by space weathering. *Nature Communications*, *11*(1), 1117. https://doi.org/10.1038/s41467-020-14758-3

Matsumoto, T., Noguchi, T., Tobimatsu, Y., Harries, D., Langenhorst, F., Miyake, A., & Hidaka, H. (2021). Space weathering of iron sulfides in the lunar surface environment. *Geochimica et Cosmochimica Acta*, *299*, 69–84. https://doi.org/10.1016/j.gca.2021.02.013

Matsumoto, T., Tsuchiyama, A., Miyake, A., Noguchi, T., Nakamura, M., Uesugi, K., et al. (2015). Surface and internal structures of a space-weathered rim of an Itokawa regolith particle. *Icarus*, *257*, 230–238. https://doi.org/10.1016/j.icarus.2015.05.001

Muto, S., & Enomoto, N. (2005). Substructures of gas-ion-irradiation-induced surface blisters in silicon studied by cross-sectional transmission electron microscopy. *Materials Transactions*, *46*(10), 2117–2124. https://doi.org/10.2320/matertrans.46.2117

Noguchi, T., Kimura, M., Hashimoto, T., Konno, M., Nakamura, T., Zolensky, M. E., et al. (2014). Space weathered rims found on the surfaces of the Itokawa dust particles. *Meteoritics & Planetary Sciences*, *49*(2), 188–214. https://doi.org/10.1111/maps.12111

Noguchi, T., Nakamura, T., Kimura, M., Zolensky, M. E., Tanaka, M., Hashimoto, T., et al. (2011). Incipient space weathering observed on the surface of Itokawa dust particles. *Science*, *333*(6046), 1121–1125. https://doi.org/10.1126/science.1207794

Pieters, C. M., & Noble, S. K. (2016). Space weathering on airless bodies. *Journal of Geophysical Research: Planets*, *121*(10), 1865–1884. https://doi.org/10.1002/2016JE005128

Pieters, C. M., Taylor, L. A., & Noble, S. K. (2000). Space weathering on airless bodies: Resolving a mystery with lunar samples. *Meteoritics & Planetary Sciences*, *35*(5), 1101–1107. https://doi.org/10.1111/j.1945-5100.2000.tb01496.x

Thompson, M., Barnes, J., Blewett, D., Cahill, J., Denevi, B., Donaldson Hanna, K., et al. (2021). Space weathering across the solar system: Lessons from the Moon and outstanding questions. *Bulletin of the American Astronomical Society*, *53*(4), 172. https://doi.org/10.3847/25c2cfeb.0bd09213

Thompson, M. S., Christoffersen, R., Zega, T. J., & Keller, L. P. (2014). Microchemical and structural evidence for space weathering in soils from asteroid Itokawa. *Earth Planets and Space*, *66*(1), 89. https://doi.org/10.1186/1880-5981-66-89

Tian, H.-C., Wang, H., Chen, Y., Yang, W., Zhou, Q., Zhang, C., et al. (2021). Non-KREEP origin for Chang'e-5 basalts in the Procellarum KREEP Terrane. *Nature*, *600*(7887), 59–63. https://doi.org/10.1038/s41586-021-04119-5

Wirth, B. D. (2007). How does radiation damage materials? *Science*, *318*(5852), 923–924. https://doi.org/10.1126/science.1150394

Yang, W., & Lin, Y. (2021). New lunar samples returned by Chang'E-5: Opportunities for new discoveries and international collaboration. *The Innovation*, *2*(1), 100070. https://doi.org/10.1016/j.xinn.2020.100070

Zhang, P., Tai, K., Li, Y., Zhang, J., Lantz, C., Hiroi, T., et al. (2022). Diverse space weathering effects on asteroid surfaces as inferred via laser irradiation of meteorites. *Astronomy & Astrophysics*, *659*, A78. https://doi.org/10.1051/0004-6361/202142590

Zhang, S., & Keller, L. (2010). A STEM-EELS study of the effect of solar-wind irradiation on the ilmenite from lunar soil. *Microscopy and Microanalysis*, *16*(S2), 1216–1217. https://doi.org/10.1017/S1431927610057053

Reference From the Supporting Information

Keller, L. P., Berger, E. L., Zhang, S., & Christoffersen, R. (2021). Solar energetic particle tracks in lunar samples: A transmission electron microscope calibration and implications for lunar space weathering. *Meteoritics & Planetary Sciences*, *56*(9), 1685–1707. https://doi.org/10.1111/maps.13732